PAPER

Sulfur-tolerant BaO/ZrO$_2$/TiO$_2$/Al$_2$O$_3$ quaternary mixed oxides for deNO$_X$ catalysis

Zafer Say,[a] Oana Mihai,[bc] Merve Tohumeken,[a] Kerem Emre Ercan,[a] Louise Olsson[b] and Emrah Ozensoy*[a]

Advanced quaternary mixed oxide materials in the form of BaO/Al$_2$O$_3$/ZrO$_2$/TiO$_2$ functionalized with Pt active sites (*i.e.* Pt/BaO/AZT) were synthesized and structurally characterized *via* XRD and BET in comparison to a conventional Pt/20BaO/Al benchmark NSR/LNT catalyst. The interactions of these catalysts' surfaces with SO$_x$ and NO$_x$ gases were monitored *via in situ* FTIR and TPD. There exists a delicate trade-off between NO$_x$ storage capacity (NSC) and sulfur uptake/poisoning which is strongly governed by the BaO loading/dispersion as well as the surface structure and acidity of the support material. Flow reactor measurements performed under realistic catalytic conditions show the high NO$_x$ activity for the Pt/20BaO/AZT catalyst at 573 K. After sulfur poisoning and subsequent regeneration at 773 and 973 K, Pt/20BaO/AZT surpassed the NO$_x$ catalytic performance at 573 K of all other investigated materials including the conventional Pt/20BaO/Al benchmark catalyst.

Introduction

Emission of hazardous pollutants such as CO, SO$_2$, NO$_x$, particulate matter (PM) and unburned hydrocarbons from stationary and mobile sources is being regulated with increasingly stringent limitations.[1–3] Therefore, catalytic air pollution abatement technologies strive to minimize exhaust emission levels *via* designing novel catalytic materials. NO$_x$ storage and reduction (NSR) or the so called Lean NO$_x$ Trap (LNT) technology is a promising deNO$_x$ catalytic technology for tail pipe emission control.[4,5] The conventional catalyst that is used in NSR/LNT applications is Pt/BaO/Al$_2$O$_3$. In the past few years, the NSR/LNT technology (namely, the storage component, *i.e.* BaO/Al$_2$O$_3$) has also been coupled with conventional selective catalytic reduction (SCR) materials such as Fe-ZSM-5[6] and Fe-BEA[7] in order to increase the NO$_x$ removal efficiency by using the ammonia produced in the rich period over the LNT in the SCR catalyst. NSR/LNT material systems are known to have three major challenges associated with NO$_x$ storage capacity (NSC), sulfur poisoning and thermal aging.[1,2,8–11] Since NO$_2$(g) and SO$_2$(g) are acidic adsorbates, they compete for similar adsorption sites on the catalyst surface. Therefore, improvement of the sulfur tolerance of an

NSR/LNT system needs to be accomplished without compromising the NO$_x$ storage capacity. Along these lines, in our former studies we have focused on the design, synthesis and characterization of a variety of binary and ternary mixed metal oxide systems which are promoted with reducible oxides such as Fe$_2$O$_3$/Fe$_3$O$_4$,[12] TiO$_2$,[9,13–16] CeO$_2$,[8,17] and ZrO$_2$.[18] For instance, we have demonstrated that CeO$_2$ is an effective promoter enabling a significant improvement in the NO$_x$ reduction and sulfur regeneration of NSR/LNT catalysts.[8,17] On the other hand, while TiO$_2$ promotion facilitates the sulfur release from a poisoned NSR/LNT catalyst,[9,16] due to the strong interaction between TiO$_2$ and BaO domains, BaO can diffuse into TiO$_2$, forming complex mixed oxides leading to thermal aging and deactivation.[13–15] It is worth mentioning that as a result of its moderately high surface acidity and lower specific surface area, pure TiO$_2$ has a typically lower SO$_x$ and NO$_x$ uptake than that of γ-Al$_2$O$_3$.[19–22] However, there exist opportunities to design novel mixed oxide systems that can simultaneously exhibit high NSC, thermal stability and sulfur tolerance. In order to explore such prospects, ZrO$_2$ and TiO$_2$ containing complex oxide architectures can be utilized. By altering the composition and crystal structure of such mixtures as well as by utilizing the well-known stabilizing influence of ZrO$_2$ on TiO$_2$[22,23] and by fine-tuning the surface acidity,[24–26] promising material alternatives can be synthesized. One of the critical aspects to be considered in such efforts is the relatively low thermal stability of ZrO$_2$/TiO$_2$ binary mixed oxides. In one of our recent reports, structural evolution of ZrO$_2$/TiO$_2$ and Al$_2$O$_3$/ZrO$_2$/TiO$_2$ mixed oxides was followed as a function of temperature by means of X-ray

[a] *Department of Chemistry, Bilkent University, 06800 Ankara, Turkey.*
E-mail: ozensoy@fen.bilkent.edu.tr
[b] *Chemical Reaction Engineering and Competence Centre for Catalysis, Chalmers University of Technology, SE-412 96 Göteborg, Sweden*
[c] *Department of Petroleum Processing Engineering and Environmental Protection, Petroleum-Gas University of Ploiesti, 39 Bucuresti Blvd., 100680 Ploiesti, Romania*

This journal is © The Royal Society of Chemistry 2017

Catal. Sci. Technol., 2017, 7, 133–144 | 133

Diffraction (XRD), Raman spectroscopy and Brunauer–Emmett–Teller (BET) specific surface area analysis techniques.[18] The amorphous ZrO_2/TiO_2 material obtained after the synthesis readily crystallizes at temperatures higher than 773 K to form ordered and low surface area structures such as $ZrTiO_4$ and tetragonal zirconia (i.e. t-ZrO_2). On the other hand, disordered (amorphous-like) $Al_2O_3/ZrO_2/TiO_2$ persists even at 1173 K revealing a relatively higher NO_x uptake than that of binary ZrO_2/TiO_2.[18] ZrO_2/TiO_2 and $Al_2O_3/ZrO_2/TiO_2$-based materials were also investigated in terms of their composition, thermal stability, NO_x storage capability and sulfur uptake/regeneration characteristics by the Toyota Motor Company.[27–31] ZrO_2/TiO_2 with a mass ratio of 70 : 30 was claimed to have the highest tolerance against sulfur poisoning[30] and the influence of the Al_2O_3 on NO_x storage capacity, structural integrity, sintering resistance, and thermal deterioration has been demonstrated.[27] NO_x storage and sulfur tolerance of similar NSR catalysts (i.e. Pt/Rh/Ba/K/AZT and titanium doped-AZT)[28,29] were also studied. In addition, Zou et al. investigated the influence of the mass ratio of Al_2O_3 : ZrO_2–TiO_2 on the performance of the Pt/K/AZT LNT catalyst and reported that a mass ratio of 1 : 1 revealed the best performance after sulfur poisoning.[32]

In the current study, we focus on the SO_x adsorption and SO_x reduction/regeneration/release properties of ternary ($Al_2O_3/ZrO_2/TiO_2$, AZT) and quaternary (BaO/$Al_2O_3/ZrO_2/TiO_2$, BaO/AZT) mixed oxide systems functionalized with redox active Pt sites in comparison to a benchmark NSR/LNT catalyst (i.e. Pt/BaO/Al_2O_3) via in situ Fourier Transform Infrared Spectroscopy (in situ FTIR), Temperature Programmed Desorption (TPD), XRD and BET surface area analysis techniques. In addition to these detailed spectroscopic studies on catalytic powders, using a flow reactor operated under realistic catalytic conditions, quantitative NO_x storage capacities of the synthesized materials prepared in a monolithic form are also investigated after sulfur poisoning and subsequent regeneration. The current study reveals a molecular level insight into the poisoning, regeneration and the competition between NO_x and SO_x species for the adsorption sites of complex NSR/LNT catalysts.

Experimental

Material synthesis

Detailed information regarding the synthesis procedures of $Al_2O_3/ZrO_2/TiO_2$ (AZT, Al_2O_3 : ZrO_2 : TiO_2 = 50 : 35 : 15, by mass) can be found in one of our recent reports.[18] The Pt/AZT material was prepared via a wetness impregnation method utilizing $Pt(NH_3)_2(NO_2)_2$ (Aldrich, diamminedinitritoplatinum(II), 3.4 wt% solution in dilute NH_3(aq)). Before the incorporation of 1 wt% Pt, the $Al_2O_3/ZrO_2/TiO_2$ support material was initially calcined in air at 973 K for 150 min in order to remove carbonaceous species and organic precursors.

Pt/BaO/AZT catalysts with 8 or 20 wt% BaO loading (i.e. Pt/8BaO/AZT and Pt/20BaO/AZT, respectively) were prepared by wetness impregnation of the $Al_2O_3/ZrO_2/TiO_2$ support

(which was initially calcined at 973 K for 150 min) with an aqueous solution of barium nitrate ($Ba(NO_3)_2$, ACS Reagent, ≥99%, Riedel-de Häen, Germany). This is followed by calcination at 873 K in air for 150 min to remove the nitrate/nitrite content by thermal decomposition. Next, these materials were impregnated with the aforementioned platinum precursor to obtain 1 wt% nominal precious metal loading. Finally, obtained samples were calcined in air at 973 K for structural stabilization as well as the elimination of nitrate/nitrite and organic functionalities. For the synthesis of the Pt/20BaO/Al benchmark catalyst, the γ-Al_2O_3 support (i.e. SASOL Puralox, 210 m^2 g^{-1}) is impregnated with an aqueous solution of barium nitrate, which is followed by calcination at 873 K in air for 150 min. Finally, 20BaO/Al_2O_3 was impregnated with the $Pt(NH_3)_2(NO_2)_2$ precursor to obtain a 1 wt% nominal precious metal loading.

Material characterization

Details regarding the XRD, BET surface area analysis, TPD and in situ FTIR measurements can be found in our former reports.[9,13,14,17,18,33,34] Transmission electron microscopy (TEM) analysis of the Pt/8BaO/AZT catalyst was performed using a FEI Titan 80-300 with a probe C_s corrector operating at 300 kV. Images were acquired in the STEM mode using a HAADF detector.

Transmission mode in situ FTIR measurements were performed in a custom-designed batch-type spectroscopic reactor coupled to an FTIR spectrometer (Bruker Tensor 27) and a quadrupole mass spectrometer (QMS, Stanford Research Systems, RGA 200) for TPD analysis. All of the FTIR spectra were acquired at 323 K.

The sulfur desorption/regeneration characteristics of each material were investigated by exposing the pre-poisoned (2.0 Torr of a SO_2 + O_2 gas mixture, SO_2 : O_2 = 1 : 10, at 673 K for 5 min, SO_2 purity >99%, air products, O_2 purity >99.999%, Linde GmbH) catalyst surfaces to 15.0 Torr of H_2(g) (H_2 purity >99.999%, Linde GmbH) at 323 K. Next, catalyst surfaces were annealed at 473 K, 673 K, 773 K or 973 K in the presence of H_2(g) for 5 min. Finally, the catalysts were cooled to 323 K in the reducing gas environment and FTIR spectra were acquired.

SO_2 and NO_x competitive adsorption experiments were performed at 323 K with and without SO_2(g). Initially, samples were saturated with a 2.0 Torr NO_2(g) exposure over the samples for 10 min at 323 K. NO_2(g) was prepared by mixing NO(g) (air products, 99.9%) and excess O_2(g) (Linde GmbH, Germany, 99.999%). After the acquisition of the FTIR spectrum at 323 K in the presence of NO_2(g), the spectroscopic reactor was evacuated to a pressure less than 10^{-3} Torr and surfaces were flash-annealed to 973 K in order to remove adsorbed surface species and regenerate/clean the surface. Next, 2 Torr NO_2(g) and 0.4 Torr SO_2(g) were simultaneously introduced over the sample for 10 min at 323 K and FTIR spectra were acquired in the presence of the gas mixture.

Prior to SO_2 TPD experiments, material surfaces were exposed to 2.0 Torr of a SO_2 + O_2 gas mixture (SO_2 : O_2 = 1 : 10)

134 | Catal. Sci. Technol., 2017, 7, 133–144

This journal is © The Royal Society of Chemistry 2017

at 673 K for 30 min. Then, the reactor was evacuated to a pressure lower than 10^{-3} Torr, followed by heating under vacuum up to 1173 K with a linear heating ramp of 12 K min^{-1}. During the TPD experiments, m/z = 32 (corresponding to O_2(g) desorption in addition to S(g) formation due to the impact ionization-induced fragmentation of SO_2(g) species in QMS) and m/z = 64 (corresponding to SO_2(g) desorption) channels were monitored. It is worth mentioning that the contribution from S(g) species to the m/z = 32 desorption channel of the current TPD spectra is rather limited, as the mass spectrum of pure SO_2(g) reveals a m/z = 64 : m/z = 32 intensity ratio of 10 : 1.

Pyridine adsorption experiments were carried out by saturating the catalyst surfaces with pyridine (pyridine, anhydrous, purity >99.8%, Sigma, Aldrich) vapour at 298 K for 15 min, followed by subsequent evacuation ($P < 5 \times 10^{-2}$ Torr) in order to eliminate vibrational features associated with gas phase and weakly adsorbed species.

NH_3-TPD measurements were performed *via* a Setaram Sensys Digital Scanning Calorimeter (DSC). Two quartz tubes were mounted inside the DSC. In one tube, *ca.* 60 mg of catalyst powder was placed on a sintered quartz plate, while the other tube was used as a reference. The outlet products were analyzed using a Hiden HPR-20 QUI mass spectrometer. The total flow rate used in all of the NH_3 TPD experiments was 20 ml min^{-1}, which was taken from a larger gas flow and the excess gas was sent to ventilation. Argon was used as an inert balance in these experiments. The catalysts were first degreened at 923 K, using 0.9% H_2 for 30 min. The samples were then exposed to Ar for 5 min, followed by a gas mixture (474 ppm NO, 4.5% O_2, 4.8% CO_2) balanced with Ar at the same temperature for 2 h. After degreening, the catalysts were oxidized and reduced at 873 K by exposing them to 8% O_2 for 30 min and 0.9% H_2 for 1 h, respectively. Argon was flushed between these two steps. NH_3-TPD experiments were performed after pre-treatment and the catalysts were exposed to 2000 ppm NH_3 at 323 K for 8 h. Thereafter, the samples were treated with argon for 30 min and the temperature was increased to 1073 K with a ramp speed of 5 °C min^{-1} in the presence of an Ar(g) flow.

Catalytic reactions

The NO_x storage effects on BaO and support materials induced by SO_2 exposure and sulfur regeneration were studied in detail using the monolith samples in the flow reactor system. The monoliths (length = 20 mm, diameter = 21 mm, cell density of 400 cpsi) were cut from a commercial honeycomb cordierite structure and calcined at 773 K for 2 h. The calcined monoliths were then wash-coated with the powder catalysts of Pt/AZT, Pt/8BaO/AZT, Pt/20BaO/AZT, Pt/20BaO/Al. In the next step, the monoliths were immersed into a slurry which consisted of a liquid phase (with equal volumes of distilled water and ethanol) and a solid phase (with 5 wt% boehmite and 95 wt% powder catalyst). The solid in the slurry was 20 wt%. The excess liquid was gently blown away and the mono-

lith was dried at 363 K for 2 min. The immersing, blowing away and drying were repeated several times until the weight of the washcoat was about 700 mg, followed by their calcination at 823 K for 2 min in air. Finally, the washcoated monoliths were calcined at 873 K for 2 h in an oven.

The sulfur poisoning, regeneration and the storage/reduction cycles were carried out in a horizontally mounted quartz tube flow reactor, heated by a heating wire controlled by a Eurotherm temperature-controller. The gas temperature was measured and controlled by a thermocouple positioned about 10 mm in front of the monolith, while the catalyst temperature was measured by another thermocouple inserted in the center channel of the monolith. The inlet gas feed was regulated using several Bronkhorst mass flow controllers. Water in the form of steam was introduced into the reactor by a controlled evaporation and mixing system (Bronkhorst Hi-Tech). All lines were heated and maintained at 473 K in order to prevent water condensation. The effluent species from the reactor were analyzed by a gas phase FTIR spectrometer (MKS Instruments, MultiGas 2030) with the gas cell heated to 464 K.

In order to get a constant catalytic behaviour of the samples during measurements, the calcined monoliths were first degreened at 923 K. During degreening, the samples were exposed to 1% H_2 for 30 min, then the samples were flushed with Ar for 5 min, and a gas mixture (500 ppm NO, 5% O_2, 5% CO_2, 5% H_2O), balanced with Ar at the same temperature for 2 h, was used. After degreening, the samples were subjected to the stability tests at 573 K where eleven successive lean/rich cycles (7 cycles with NO in the feed and 4 cycles with NO_2, in the presence of 5% CO_2, 5% H_2O, and 10% O_2 (for the lean step) and 1% H_2 (for the rich step) were performed. The duration of each lean cycle was 4 min, while for the rich step was 1 min. The cycles described above were denoted in this study as a single set of stability test. This set was repeated three times for Pt/20BaO/Al, Pt/20BaO/AZT and Pt/AZT. The Pt/8Ba/AZT catalyst was subjected to additional three stability sets, since it was not completely stable after three sets. The samples were pre-treated at 773 K between two consecutive stability test sets according to the following procedures: (a) the samples were first reduced with a gas mixture of 1% H_2, 5% CO_2 and 5% H_2O for 15 min; (b) exposed to 5% CO_2, 5% H_2O and Ar for 5 min; and (c) oxidized in 5% O_2, 5% CO_2 and 5% H_2O for 15 min.

After the stability tests, the samples were subjected to NO_x experiments where successive lean/rich cycles (7 cycles with NO in the feed and 4 cycles with NO_2) at three different temperatures of 673, 573 K and 473 K were carried out (only NO_x results at 573 K are shown in this study). The pre-treatment reported above was conducted before starting the NO_x cycling tests.

SO_2 poisoning was investigated by exposing the samples to a sulfur-containing gas mixture where lean and rich cycles were alternated. For the SO_2 poisoning tests, the temperature was decreased to 573 K after pre-treatment at 773 K and ten successive lean/rich cycles were conducted according to the

This journal is © The Royal Society of Chemistry 2017

Catal. Sci. Technol., 2017, **7**, 133–144 | 135

following procedure: (1) lean cycle: 30 ppm SO_2, 500 ppm NO, 10% O_2, 5% CO_2 and 5% H_2O for 4 min and (2) rich cycle: 30 ppm SO_2, 500 ppm NO, 1% H_2, 5% CO_2 and 5% H_2O for 1 min.

The sulfur regeneration of the catalysts was investigated and the samples were regenerated at 773 and 973 K in a gas mixture of 1% H_2, 5% CO_2 and 5% H_2O for 1 h. After the regeneration, the samples, which were pre-treated (as reported above) and subjected to 7 lean/rich cycles at 573 K, contained NO + O_2 + CO_2 + H_2O (during the lean step) and NO + H_2 + CO_2 + H_2O (during the rich step).

Results and discussion

The structures of the synthesized catalysts were characterized by means of XRD and BET analysis. Fig. 1 illustrates the XRD patterns of Pt/AZT, Pt/8BaO/AZT, Pt/20BaO/AZT, Pt/20BaO/Al and Pt/20BaO/ZT recorded after calcination in air at 973 K for 150 min. The Pt/AZT catalyst in Fig. 1 exhibits highly amorphous characteristics except the presence of metallic platinum features (JCPDS 001-1190). Incorporation of 8 wt% BaO does not reveal any additional ordered phases except the attenuation of the platinum diffraction signals. This trend is also observable for the catalyst with a higher BaO loading, i.e. Pt/20BaO/AZT. It is likely that the presence of BaO domains on the AZT support hinders the precious metal sintering and facilitates the metal dispersion. XRD analysis of the benchmark NSR/LNT catalyst (i.e. Pt/20BaO/Al$_2$O$_3$) revealed γ-Al$_2$O$_3$ (JCPDS 001-1303), BaAl$_2$O$_4$ (JCPDS 017-0306) and metallic Pt (JCPDS 001-1190) features. On the Pt/20BaO/Al catalyst, BaO domains interact with the γ-Al$_2$O$_3$ support at elevated temperatures yielding the formation of the undesired BaAl$_2$O$_4$ phase due to thermal aging.[13,14,17] On the other hand, BaAl$_2$O$_4$ is not visible for the AZT containing samples (Fig. 1). Pt/20BaO/ZT reveals various discernible diffraction signals, namely, t-ZrO$_2$ (JCPDS 80-2155), ZrTiO$_4$ (JCPDS 34-415) and BaTiO$_3$ (JCPDS 34-0129). In light of these findings, it is apparent that alumina acts as a diffusion barrier between BaO, ZrO$_2$ and TiO$_2$ domains hindering the formation of BaTiO$_3$, ZrTiO$_4$ and other crystalline phases on the Pt/20BaO/AZT catalyst.

This observation is also consistent with the ca. ten-fold difference between the specific surface area (SSA) values of AZT versus ZT as shown in Table 1.

Furthermore, the SSA of Pt/8BaO/AZT and Pt/20BaO/AZT catalysts are rather comparable to that of the benchmark Pt/20BaO/Al catalyst while Pt/AZT, which lacks the BaO component, has a higher SSA resembling that of the AZT support material. In the absence of the Al$_2$O$_3$ component (i.e. for the Pt/20BaO/ZT catalyst), SSA was found to be significantly low (23 m^2 g^{-1}). Fig. 2 shows a high angle annular dark field scanning transmission electron microscopy (HAADF-STEM) image of the Pt/8BaO/AZT catalyst where the bright features correspond to Pt-nanoparticles. HAADF-STEM images suggest that the typical Pt particle size varies within 2–8 nm, albeit smaller Pt particles are also visible.

Sulfur adsorption and reduction characteristics of synthesized materials were studied as a function of temperature by means of in situ FTIR. Fig. 3a–d present in situ FTIR data for the regeneration of the sulfur-poisoned Pt/AZT, Pt/8BaO/AZT, Pt/20BaO/AZT and Pt/20BaO/Al catalyst surfaces with H_2(g) at various temperatures. For these set of experiments, the catalysts were initially saturated with 2.0 Torr of a SO_2 + O_2 gas mixture (SO_2 : O_2 = 1 : 10) at 673 K and then cooled to 323 K followed by the evacuation of the spectroscopic reactor. Next, H_2(g) was introduced at 323 K and the catalysts were exposed to H_2(g) at the given temperatures. Note that the currently utilized temperature for sulfur poisoning (i.e. 673 K) is compatible with realistic NSR operational temperatures, enabling severe poisoning of the catalyst surface. In situ FTIR spectra acquired immediately after the sulfur poisoning at 673 K (data not shown here) and after the H_2(g) introduction at 323 K were identical to that of the topmost spectra given in Fig. 3. In other words, H_2(g) exposure at 323 K had no detectable influence on the vibrational features of the SO$_x$ species residing on the catalyst surfaces.
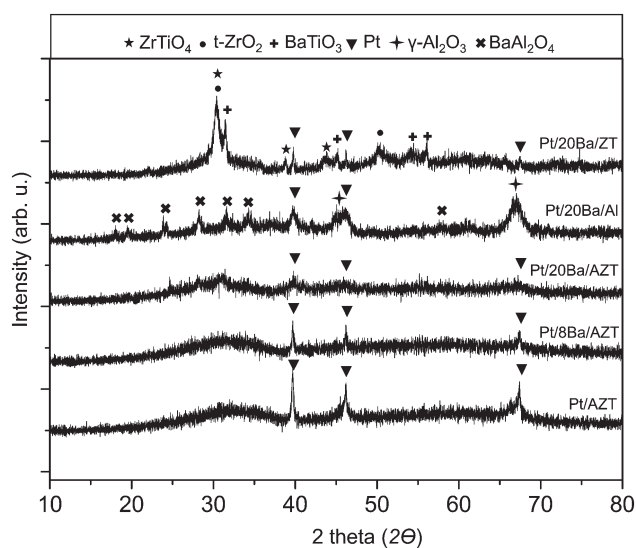

Fig. 1 XRD patterns corresponding to Pt/AZT, Pt/8BaO/AZT, Pt/20BaO/AZT, Pt/20BaO/Al and Pt/20BaO/ZT powder catalysts after calcination at 973 K.

Table 1 BET specific surface area values for the investigated materials

Materials	S_{BET}^{a} (m^2 g^{-1})
ZT	26
AZT	230
Pt/AZT	191
Pt/8BaO/AZT	152
Pt/20BaO/AZT	132
Pt/20BaO/Al	134
Pt/20BaO/ZT	23

^{a} All of the materials were calcined at 973 K for 150 min.

136 | Catal. Sci. Technol., 2017, **7**, 133–144

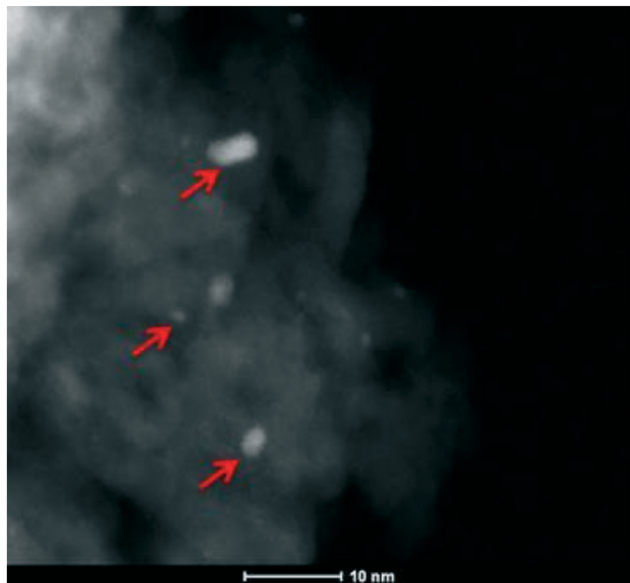This journal is © The Royal Society of Chemistry 2017

Fig. 2 HAADF-STEM image of the Pt/8BaO/AZT catalyst. Some of the Pt-nanoparticles are marked with arrows.

In Fig. 3a, it is seen that at the beginning of the reduction series (*i.e.* after 323 K $H_2(g)$ exposure), the SO_x-saturated Pt/AZT ternary oxide reveals two main features at 1391 and 1027 cm^{-1}. Although these vibrational features are fairly difficult to analyse due to their highly convoluted nature, they can be attributed to the antisymmetric and symmetric vibration modes of surface sulfates (SO_4^{2-}), respectively.[8,9,35–37] These results are in good agreement with Kantcheva *et al.*[38] who reported a detailed study on the SO_2 interaction with ZrO_2 surfaces revealing similar FTIR spectral features to that of Pt/AZT. The Pt/AZT ternary oxide system was modified by the incorporation of BaO domains serving as NO_x storage functionalities with different mass percentiles (*i.e.* 8 and 20 wt% BaO) and analyzed in an analogous manner.

The *in situ* FTIR spectra in Fig. 3b and c present the SO_x reduction characteristics of the poisoned Pt/8BaO/AZT and Pt/20BaO/AZT catalysts, respectively, while Fig. 3d shows the corresponding results for the conventional NSR catalyst (*i.e.* Pt/20BaO/Al) as the benchmark sample. It is clear that the incorporation of basic BaO domains onto the AZT ternary oxide system (*i.e.* 323 K spectra in Fig. 3b–d) results in different spectral line shapes in the *in situ* FTIR data from that of the BaO-free sample (323 K spectrum in Fig. 3a).

It can be seen in Fig. 3b–d that adsorption geometries of SO_x species on BaO-containing catalysts immediately after poisoning (*i.e.* spectra corresponding to 323 K in Fig. 3b–d) are rather similar as evidenced by the analogous vibrational features observed for these samples. The topmost FTIR spectra displayed in Fig. 3b–d reveal four main vibrational features at *ca.* 1370, 1250, 1160 and 1040 cm^{-1}. While the vibrational signatures at 1250 and 1160 cm^{-1} can be attributed to bulk-like sulfates on BaO (*i.e.* $BaSO_4$), the remaining two features can be assigned to surface sulfate/sulfite groups located on the BaO domains or residing on the support surface (*i.e.*
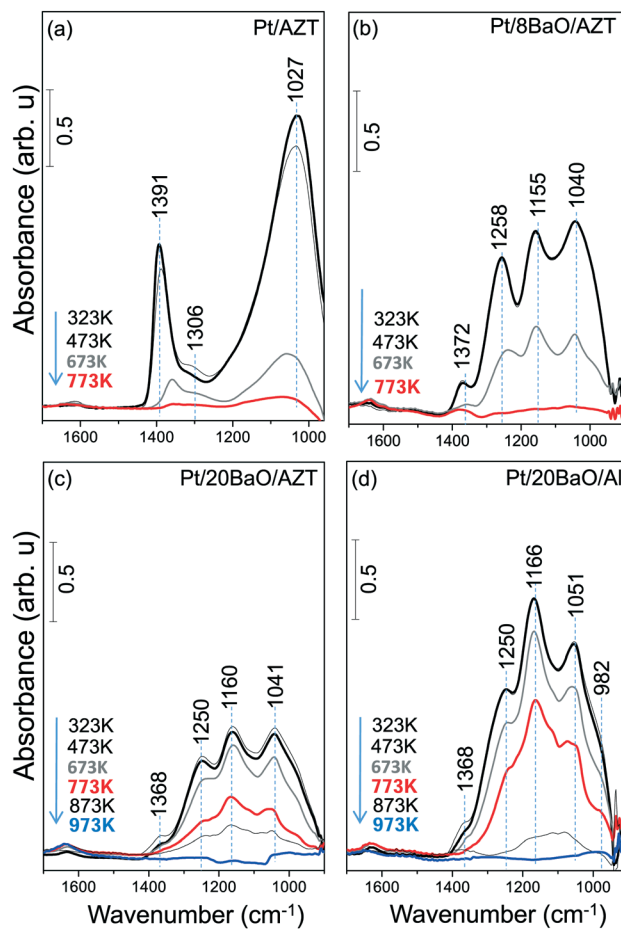

Fig. 3 FTIR spectra related to SO_x regeneration properties of (a) Pt/AZT, (b) Pt/8BaO/AZT, (c) Pt/20BaO/AZT and (d) Pt/20BaO/Al. All powder catalysts were initially sulfated (2.0 Torr, $SO:O_2 = 1:10$ for 15 min at 673 K) and then exposed to $H_2(g)$ (15.0 Torr) at 323, 473, 673, 773, 873 and 973 K for 5 min. All spectra were recorded at 323 K in the presence of $H_2(g)$.

AZT or γ-Al_2O_3).[8,9,39] In addition to these features, rather convoluted vibrational signatures can be detected as a shoulder at 970–980 cm^{-1} corresponding to surface sulfites (SO_3^{-2}).[8,9,35–38]

Fig. 3 suggests that within the temperature range of 323–473 K and in the presence of excess $H_2(g)$, SO_x species on the investigated catalysts are relatively stable. However, above 473 K, sulfate/sulfite groups start to react with $H_2(g)$, possibly forming $H_2S(g)$. $H_2S(g)$ evolution was reported in our former TPD studies on SO_x-poisoned γ-Al_2O_3, TiO_2 (anatase) as well as TiO_2/Al_2O_3 binary oxide surfaces.[9] However it is likely that the generated $H_2S(g)$ in the current experiments is below the detection limit of the utilized FTIR spectroscopic cell. Increasing the temperature to 673 K in the presence of $H_2(g)$ causes a significant attenuation of all of the SO_x-related vibrational features of the Pt/AZT catalyst (Fig. 3a), where the complete regeneration can be achieved at 773 K (bottommost/red spectrum in Fig. 3a). Fig. 3b indicates that as in the case of Pt/AZT, complete SO_x elimination from the surface

can also be achieved for Pt/8BaO/AZT at $T \geq 773$ K. On the other hand, for Pt/20BaO/AZT and the Pt/20BaO/Al benchmark catalyst, complete sulfur elimination in the presence of $H_2(g)$ occurs only at $T \geq 973$ K (bottommost/blue spectra in Fig. 3c and d). The differences in the relative thermal stabilities of the SO_x species which formed on the Pt/AZT, Pt/8BaO/AZT, Pt/20BaO/AZT and Pt/20BaO/Al catalysts will be further discussed in the next section along with the TPD experiments.

Fig. 3 suggests that the Pt/AZT ternary oxide catalyst shows better sulfur regeneration characteristics than the conventional Pt/20BaO/Al catalyst or the Pt/8BaO/AZT and Pt/20BaO/AZT catalysts. However it should be emphasized that Pt/AZT is not necessarily an ideal NSR catalyst, as the lack of a basic oxide component such as BaO in its formulation significantly limits the NSC of this material (Fig. 4). The NO_x storage and reduction properties of ZT, AZT, Pt/ZT and Pt/AZT were analyzed *via in situ* FTIR spectroscopy as well as TPD and were discussed thoroughly in a former report.[18]

The *in situ* FTIR spectrum in Fig. 4 corresponding to the Pt/AZT catalyst can be characterized by the vibrational features located at 1610, 1586, 1556, 1294 and 1245 cm^{-1} which can be assigned to various types of nitrates.[18] For the Pt/AZT catalyst, while the bands at 1610 and 1245 cm^{-1} are associated with bridging nitrates, the features at 1586, 1556 and 1294 cm^{-1} can be assigned to bidentate nitrates.[18] On the other hand, the *in situ* FTIR spectrum for the Pt/20BaO/Al benchmark sample given in Fig. 4 reveals vibrational features at 1610 and 1245 cm^{-1} (bridging surface nitrates), 1560 (bidentate and/or monodentate surface nitrates) as well as at 1330 and 1420 cm^{-1} (bulk/ionic nitrates).[17,18]
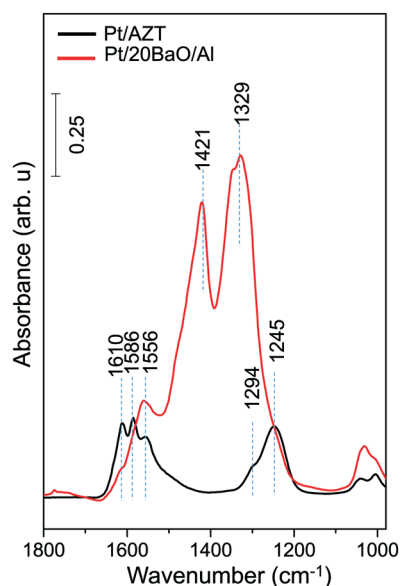

Fig. 4 FTIR spectra corresponding to Pt/20BaO/Al (red spectrum) and Pt/AZT (black spectrum) powder catalysts after 5.0 Torr NO$_2$ exposure at 573 K for 10 min and subsequent evacuation. All spectra were recorded at 323 K.

It is difficult to make a precise quantitative comparison of the amount of NO_x species adsorbed on Pt/AZT *versus* Pt/20BaO/Al solely based on the integrated FTIR intensities (due to the differences in the IR absorption cross sections of dissimilar oscillators and vibrational intensity transfer processes between oscillators[40]). However, one can still qualitatively argue that a Pt/AZT sample lacking any NO_x storage component (*i.e.* BaO) adsorbs a lower quantity of NO_x than the Pt/BaO/Al benchmark catalyst during the batch-mode *in situ* FTIR spectroscopic measurements described above.

TPD experiments were also carried out in order to investigate the thermal regeneration ability of the synthesized catalysts after sulfur poisoning, as well as to compare the relative adsorption strengths of SO_x species residing on the poisoned catalyst surfaces. Prior to TPD experiments, each catalyst was exposed to 2.0 Torr of a $SO_2 + O_2$ gas mixture ($SO_2 : O_2 = 1 : 10$) at 673 K for 30 min. Fig. 5a–d illustrate the TPD profiles corresponding to the pre-sulfated Pt/AZT, Pt/8BaO/AZT, Pt/20BaO/AZT and Pt/20BaO/Al catalysts, respectively. Each panel in Fig. 5 shows two major TPD desorption channels, namely, $m/z = 32$ and 64 corresponding to O_2 and SO_2 desorption, respectively. It is worth mentioning that no other desorption species such as H_2S were detectable in the TPD experiments. Fig. 5 clearly shows that SO_x species adsorbed on all of the investigated catalysts have high thermal stability, evidenced by the lack of any SO_x desorption/decomposition signals below 700 K.

On the other hand, the SO_x decomposition/desorption maxima in Fig. 5 show noticeable variations as a function of catalyst composition indicating the dissimilarities in the relative thermal stabilities of SO_x species on different catalyst surfaces. For the Pt/AZT catalyst lacking BaO (Fig. 5a), the $m/z = 32$ and 64 desorption channels reveal identical temperature maxima at 820 K. This indicates that sulfate and sulfite species decompose and desorb from the Pt/AZT surface predominantly in the form of $SO_2(g) + O_2(g)$. The results in Fig. 5a suggests that the SO_x desorption is almost complete for the Pt/AZT sample within the thermal window of TPD analysis. In contrast, when the TPD data for Pt/AZT (Fig. 5a) is compared with that of the conventional Pt/20BaO/Al benchmark catalyst (Fig. 5d), it can readily be seen that the SO_x desorption maxima shift to significantly higher temperatures extending well beyond 1050 K (*i.e.* the highest experimentally attainable temperature in the current TPD setup) with incomplete desorption, which is also further verified by the post-TPD residual sulfur analysis *via in situ* FTIR given in Fig. 6. This observation implies that the high BaO loadings lead to strong binding sites for SO_2, resulting in the formation of thermally stable sulfite and sulfate species, unlike the relatively more acidic Pt/AZT surface exhibiting weaker adsorption sites for SO_x. On the other hand, low/moderate surface coverages of BaO as in the case of Pt/8BaO/AZT do not lead to a significant increase in the thermal stability of adsorbed sulfates/sulfites.

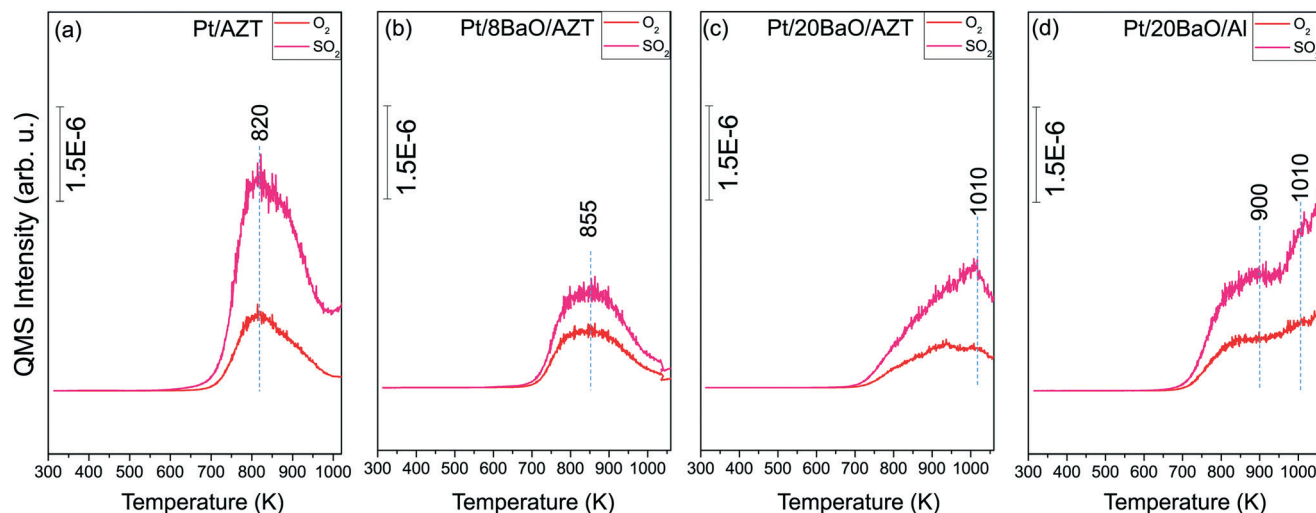Fig. 5b and c, which correspond to the TPD profiles of sulfur poisoned Pt/8BaO/AZT and Pt/20BaO/AZT catalysts,

138 | *Catal. Sci. Technol.*, 2017, **7**, 133–144

This journal is © The Royal Society of Chemistry 2017

Fig. 5   TPD profiles for (a) Pt/AZT, (b) Pt/8BaO/AZT, (c) Pt/20BaO/AZT and (d) Pt/20BaO/Al powder catalysts after 2.0 Torr SO_x (2.0 Torr SO_2 + O_2, $SO_2 : O_2$ = 1 : 10) adsorption at 673 K for 30 min.

respectively, suggest that by varying the BaO loading, one can fine-tune both the SO_x adsorption strength as well as the total amount of SO_x species adsorbed on the catalyst surfaces. Although the types of the desorbing gases (*i.e.* SO_2(g) + O_2(g)) do not change upon BaO incorporation to the Pt/AZT structure, the desorption temperature maxima monotonically shift to higher temperatures with increasing BaO loading. It can also be realized that increasing BaO loading also increases the amount of SO_x adsorbed on the catalyst surfaces which is evidenced by the greater integrated TPD signals for Pt/20BaO/
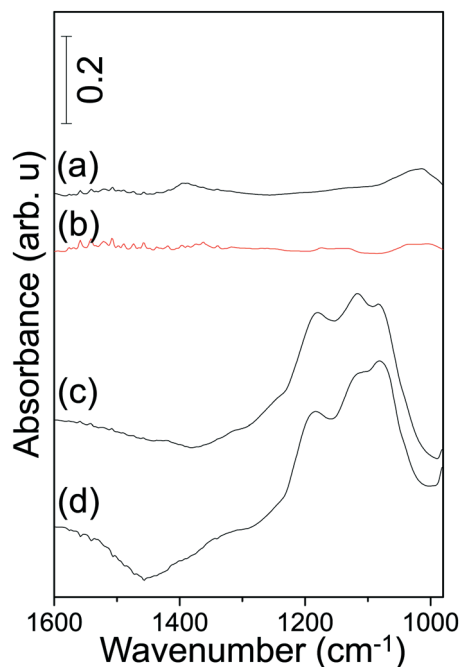

Fig. 6   FTIR spectra acquired after SO_x-TPD experiments revealing the residual sulfur species on (a) Pt/AZT, (b) Pt/8BaO/AZT, (c) Pt/20BaO/AZT and (d) Pt/20BaO/Al powder catalysts.

AZT (Fig. 5c) than that of Pt/8BaO/AZT (Fig. 5b). It should be also emphasized that the difference in the regeneration ability of two catalysts having an identical BaO loading (Pt/20BaO/AZT and Pt/20BaO/Al) can be compared by investigating the SO_x desorption signals at $T \geq 1010$ K. In this thermal window, while sulfur desorption from the Pt/20BaO/AZT surface approaches completion, Pt/20BaO/Al continues to release increasing amounts of SO_x. Assessment of the TPD results given in Fig. 5a–d indicates that the SO_x desorption temperatures and the SO_x adsorption strength increase in the following order: Pt/AZT < Pt/8BaO/AZT < Pt/20BaO/AZT < Pt/20BaO/Al. Also, the amount of adsorbed SO_x on the BaO-containing catalyst surfaces can be ranked as follows: Pt/8BaO/AZT < Pt/20BaO/AZT < Pt/20BaO/Al.

In addition, residual SO_x analysis of the corresponding materials after the TPD experiments was also performed by means of *in situ* FTIR spectroscopy in order to have an unambiguous understanding of thermal sulfur regeneration performance (Fig. 6). Fig. 6 clearly indicates that while complete sulfur removal/regeneration is achieved for Pt/AZT (Fig. 6a) and Pt/8BaO/AZT (Fig. 6b) under vacuum conditions, a significant amount of sulfate/sulfite residues remained on Pt/20BaO/AZT (Fig. 6c) and Pt/20BaO/Al (Fig. 6d) after the TPD analysis.

In order to evaluate the NO_x storage reduction (NSR) performance of the monoliths before and after exposure to the sulfur atmosphere as well as after regeneration at 773 and 973 K, the outlet NO_x concentrations were monitored on-line during the course of seven lean/rich cycles in the presence of NO in the feed. The NO_x storage capacities were calculated by integration of the outlet NO_x concentrations with respect to the inlet amount and the obtained NSC results are depicted in Fig. 7. Fig. 7a illustrates the NSC values of fresh catalysts at 573 K as 0.024, 0.053, 0.086 and 0.062 mmol g_{cat}^{-1} for Pt/AZT, Pt/8BaO/AZT, Pt/20BaO/AZT and Pt/20BaO/Al, respectively. These results clearly point out that incorporation and
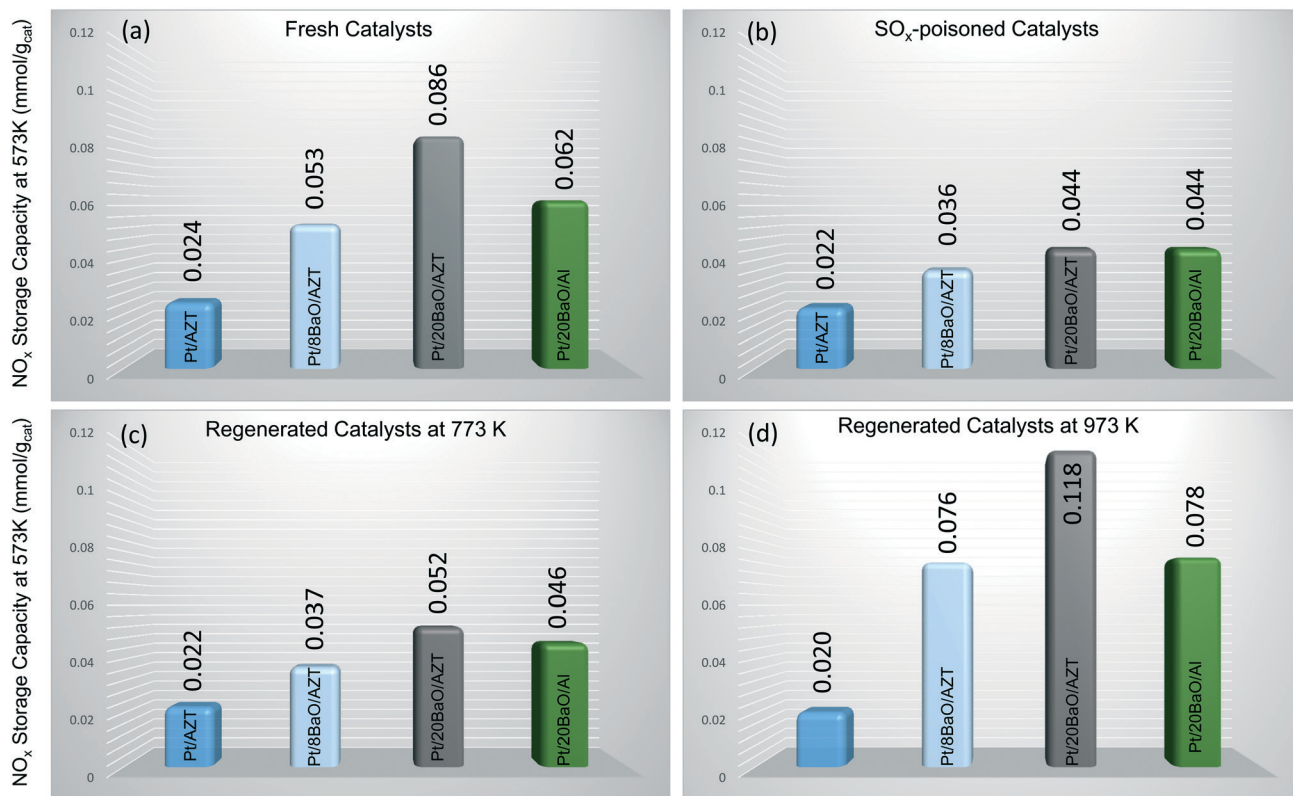
Fig. 7 NO_x storage capacities (NSC) of Pt/20BaO/Al, Pt/8BaO/AZT, Pt/20BaO/AZT and Pt/AZT monolithic catalysts obtained *via* flow-reactor experiments at 573 K with an inlet gas feed of 500 ppm NO, 5% O_2, 5% CO_2, 5% H_2O, balanced in Ar. NSC for (a) fresh catalysts, (b) after SO_x poisoning, (c) after SO_x poisoning and subsequent regeneration at 773 K, and (d) after SO_x poisoning and subsequent regeneration at 973 K.

an increase in the loading of basic BaO storage domains enhance the NSC of the investigated materials. Moreover, comparison of the Pt/20BaO/AZT and Pt/20BaO/Al materials provides an insight into the influence of the support material on the NSC. It is apparent that Pt/20BaO/AZT exhibits *ca.* 40% higher NO_x storage at 573 K than the Pt/20BaO/Al benchmark. However, at 673 K, the Pt/20BaO/Al possessed 20% higher NO_x storage than Pt/20BaO/AZT and this could possibly be related to the barium dispersion of the different samples. Sulfur poisoning of the investigated materials (excluding Pt/AZT) leads to a significant decrease in NSC as illustrated in Fig. 7b. Here, it should be noted that although the NSC of fresh Pt/AZT is almost one third of conventional Pt/20BaO/Al, it demonstrates a striking resilience against sulfur poisoning, preserving *ca.* 92% of its original NSC (*i.e.* 0.024 *vs.* 0.022 mmol g_{cat}^{-1}) after poisoning. As will be discussed in the coming sections, this can be attributed to its surface acidity (Fig. 9 and 10).

Further experiments were also carried out in order to investigate the effect of sulfur regeneration at 773 and 973 K on NSC as demonstrated in Fig. 7c and d, respectively. It can be seen in Fig. 7c that the NSC values of the Pt/AZT, Pt/8BaO/AZT, and Pt/20BaO/Al after regeneration are almost identical to that of the poisoned catalysts, revealing inefficient regeneration characteristics. On the other hand, Pt/20BaO/AZT reveals a unique behaviour where the NSC upon regeneration increases *ca.* 20% compared to its poisoned counterpart.

On the other hand, sulfur regeneration under stronger reducing conditions (*i.e.* 973 K) leads to a drastic change as illustrated in Fig. 7d. The NSC of all of the BaO-containing materials after poisoning and regeneration exhibits observably higher NSC than those of poisoned (Fig. 7b) and regenerated at 773 K (Fig. 7c) derivatives. Interestingly, under these conditions, the Pt/20BaO/AZT material reveals about 50% higher NSC than the Pt/20BaO/Al conventional benchmark catalyst and Pt/8BaO/AZT.

The increase in NSC after regeneration at 973 K (Fig. 7d) is particularly interesting. It is likely that regeneration at elevated temperatures not only facilitates the sulfur regeneration, but may also induce alterations in the material morphology and electronic structure. One of the possible origins of this observation can be associated with the precious metal sintering, which is significantly enhanced on a sulphated surface.[41] These larger Pt particles possess a higher NO oxidation ability,[42] which is consistent with the increase in the outlet NO_2 concentration after regeneration (data not shown here). The improved NO oxidation activity could be the reason for the increased NSC. Moreover, one can also speculate that the higher NSC after the regeneration at 973 K can be due to the enhancement in the surface dispersion of BaO domains in the presence of H_2.[14]

It is an important point to verify whether the results of the batch-mode *in situ* spectroscopic experiments discussed above are relevant to that of the realistic flow mode

experiments which were performed under different experimental conditions. Thus, in addition to the NSC measurements obtained under realistic flow mode conditions for the monolithic catalyst samples (Fig. 7), we also measured the relative total NO_x adsorption amounts of the synthesized powder materials in batch-mode by integrating N-containing species' desorption signals (*i.e.* NO + NO_2 + N_2 + N_2O) in NO_x-TPD experiments.

Fig. 8 shows the results of these latter experiments where we utilized the corresponding mass spectroscopic fragmentation factors for different N-containing species as described in our former publications.[18,33] The results provided in Fig. 8 clearly suggest that the NO_x adsorption capability of Pt/AZT is slightly enhanced by the addition of 8 wt% BaO. However, a higher BaO loading (*i.e.* Pt/20BaO/AZT) leads to a drastic change where the total integrated NO_x desorption signal increased by about 58% compared to that of Pt/AZT. Moreover, it was found that the NO_x adsorption performance of Pt/20BaO/AZT is 19% higher than that of benchmark NSR Pt/20BaO/Al. Comparison of the flow reactor results with the batch-mode vacuum experiments presented in Fig. 7a and 8 relating to NO_x storage exhibits an excellent correlation between these two different sets of measurements carried out under different reaction conditions.

The currently presented spectroscopic and reactivity results harmoniously point to the superior NSC of the AZT-supported Pt/20BaO/AZT catalyst to that the Pt/20BaO/Al benchmark at 573 K. It is important to investigate whether the relative surface acidities of the currently studied catalysts present any useful correlations that can elucidate the catalytic activity and poisoning characteristics. Along these lines, the surfaces of the currently examined catalysts were exposed to pyridine at 298 K in order to titrate various surface acidic sites (*i.e.* Brønsted and/or Lewis sites) and the adsorption process was monitored *via in situ* FTIR spectroscopy (Fig. 9).
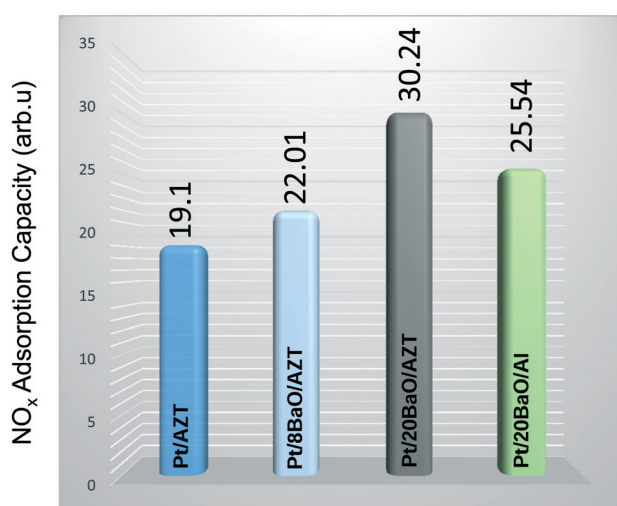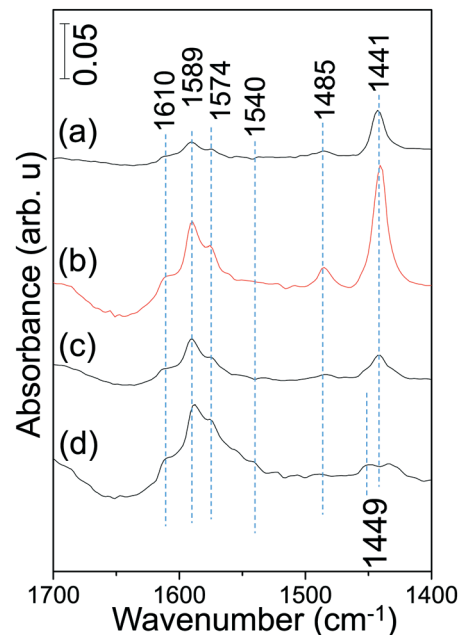

Fig. 9 *In situ* FTIR spectra corresponding to pyridine adsorption on (a) Pt/AZT, (b) Pt/8BaO/AZT, (c) Pt/20BaO/AZT and (d) Pt/20BaO/Al powder catalysts at 298 K (see the text for details).

As shown in Fig. 9, pyridine adsorption at 298 K reveals six different vibrational features located at *ca.* 1610, 1589, 1574, 1540, 1485 and 1441 cm^{-1}. Among these typical vibrational signatures, while 1610, 1485 and 1441 cm^{-1} can be attributed to the C–C stretch of a coordinatively-bonded pyridine–surface complex indicating the presence of Lewis acid sites, 1540 cm^{-1} can be assigned to the C–C stretching vibration of the pyridinium ion associated with the presence of surface Brønsted acid sites.[40,43] It should be noted that the feature located at 1485 cm^{-1} can be associated with both Lewis and Brønsted acid sites.[44,45] On the other hand, the features located at 1589 and 1574 cm^{-1} can be tentatively assigned to weakly adsorbed pyridine on Brønsted acid functionalities.[46]

Fig. 9 indicates that incorporation of 8 wt% BaO to the Pt/AZT system causes noticeable increase in the surface concentration of Lewis acid sites which is evidenced by an increase in the IR absorbance intensity of the 1441 cm^{-1} feature. However, this behavior changes at higher BaO loadings (*i.e.* for Pt/20BaO/AZT) where the relative surface coverage of Lewis acidic sites decreases discernibly. Based on these findings, it can be argued that in spite of its higher SSA of 152 m^2 g^{-1} than the Pt/20BaO/Al benchmark with a SSA of 134 m^2 g^{-1}, Pt/8BaO/AZT exhibits an extremely acidic surface, limiting its ultimate NSC. On the other hand, Pt/20BaO/AZT reveals a slightly stronger Lewis acidic character together with a weaker Brønsted acidic character than the Pt/20BaO/Al benchmark, providing a unique surface chemistry for the former catalyst that can facilitate advantageous NO_x storage and sulfur regeneration capabilities.
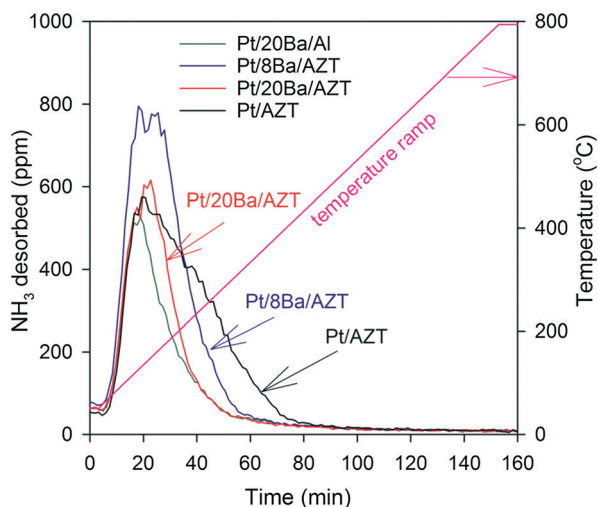

Fig. 8 Integrated NO_x TPD desorption signals for the investigated powder catalysts (see the text for details).

This journal is © The Royal Society of Chemistry 2017

Catal. Sci. Technol., 2017, **7**, 133–144 | 141

Fig. 10 NH_3-TPD profiles of Pt/AZT, Pt/8BaO/AZT, Pt/20BaO/AZT and Pt/20BaO/Al monolithic catalysts. All samples were exposed to 2000 ppm NH_3 at 323 K for 8 h during adsorption followed by an Ar(g) flow for 30 min at 323 K. TPD data were acquired in the presence of an Ar(g) flow during the temperature ramp to 1073 K.

In addition to the pyridine adsorption experiments revealing various types of surface acid sites, the total relative surface acidities of the investigated catalysts were investigated using ammonia as a probe molecule. After ammonia adsorption at 323 K, ammonia desorption profiles of the catalysts were acquired. Fig. 10 illustrates the corresponding ammonia TPD results. Ammonia desorption features in Fig. 10 located at ≥400 K can be assigned to the ammonia desorption from Lewis and/or Brønsted acid sites.[47–50] Ammonia TPD features of AZT and Al_2O_3-supported catalysts show dissimilarities. While ammonia desorption from the AZT-supported catalysts are much broader with a high temperature shoulder (reveal-

ing a variety of additional strongly acidic sites), the Al_2O_3-supported Pt/20BaO/Al benchmark catalyst presents a much sharper and weaker ammonia desorption signal that is completed at much lower temperatures, indicating the presence of a more basic surface for the latter catalyst. These results suggest that AZT-supported catalysts possess a greater total acidity than the Al_2O_3-supported Pt/20BaO/Al benchmark catalyst. Using the integrated NH_3 desorption signals given in Fig. 10, the relative total ammonia storage capacities of the investigated catalysts can be quantitatively obtained. Along these lines, the total NH_3 storage capacities were found to be 0.67, 0.58, 0.46 and 0.35 mmol g_{cat}^{-1} for Pt/AZT, Pt/8BaO/AZT, Pt/20BaO/AZT, and Pt/20BaO/Al, respectively. It is worth mentioning that these trends are in agreement with the pyridine adsorption results discussed above.

The influence of the presence of SO_2 during the NO_x adsorption was also examined *via in situ* FTIR spectroscopy at 323 K. For these experiments, synthesized catalysts were initially exposed to 2.0 Torr of NO_2 for 10 min at 323 K followed by evacuation at this temperature and acquisition of the *in situ* FTIR spectra of the NO_x-saturated surfaces. These particular spectra are shown with black color in Fig. 11 and demonstrate the higher NO_x adsorption capabilities of the clean catalyst surfaces in the absence of sulfur. Adsorption of NO_x on the fresh catalysts reveals vibrational features associated with surface and bulk nitrates as well as nitrite functionalities which have been discussed in our previous reports in detail.[13,14,17,18,33,34]

The red spectra in Fig. 11 correspond to co-adsorption of $SO_2(g)$ and $NO_2(g)$ (P_{SO_2} = 0.4 Torr, P_{NO_2} = 2.0 Torr, 10 min) on the clean catalyst surfaces at 323 K. As illustrated in Fig. 11, the red-colored spectrum in each panel contains two different families of functional groups, namely, nitrate/nitrite and sulfate/sulfite functionalities which are labelled "N" and
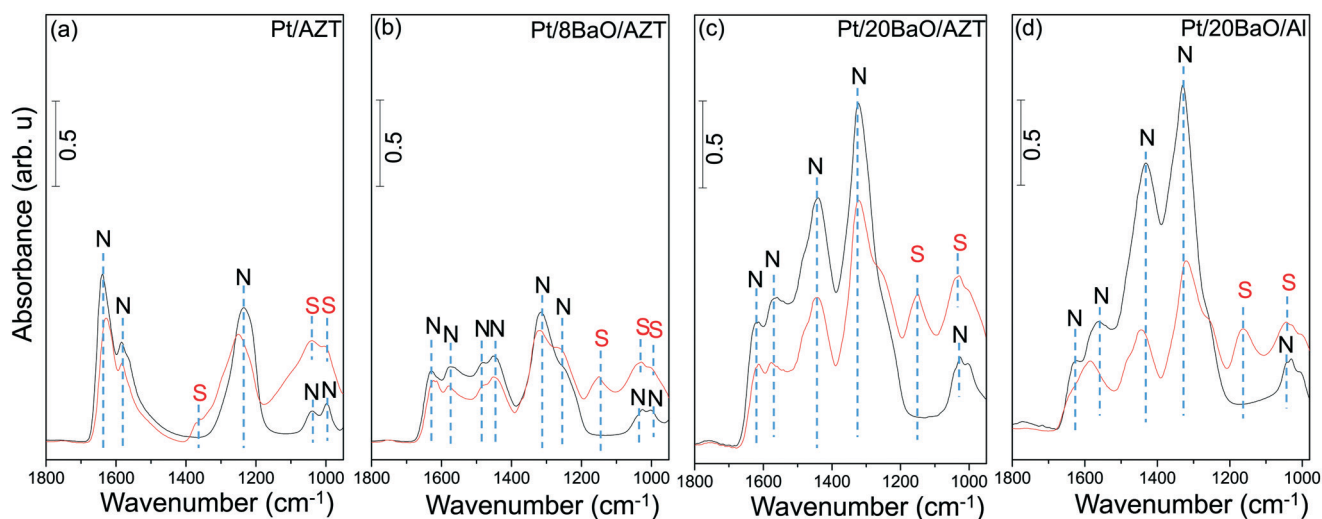

Fig. 11 FTIR spectra illustrating NO_2 adsorption properties of (a) Pt/AZT, (b) Pt/8BaO/AZT, (c) Pt/20BaO/AZT and (d) Pt/20BaO/Al powder catalysts in the presence and absence of $SO_2(g)$. The black spectra in each panel were recorded after 2.0 Torr of NO_2 exposure on fresh catalysts at 323 K for 10 min and subsequent evacuation. The red spectra in each panel correspond to simultaneous exposure of 2.0 Torr NO_2 and 0.4 Torr $SO_2(g)$ at 323 K for 10 min. 'N' and 'S' labels correspond to nitrate/nitrite and sulfate/sulfite species, respectively.

"S", respectively (Fig. 11a–d). It can be readily seen that the vibrational features obtained for the co-adsorption experiments are heavily convoluted. However, the general features of the spectral line shapes and vibrational intensities given in Fig. 11 provide valuable insights into the competition between NO_x and SO_x species for catalytic adsorption sites as well as the decline of the NO_x adsorption ability of the catalysts upon sulfur poisoning.

Fig. 11 illustrates that in the absence of the BaO domains (*i.e.* for Pt/AZT, Fig. 11a) or for low BaO loadings (*i.e.* for Pt/8BaO/AZT, Fig. 11b), NO_x vibrational features are influenced less significantly by the presence of SO_x species. On the other hand, for the catalysts with high BaO loadings, namely, Pt/20BaO/AZT and Pt/20BaO/Al, a higher sensitivity towards sulfur is visible. Particularly, for the conventional Pt/20BaO/Al benchmark catalyst (Fig. 11d), it can be realized that in the presence of sulfur, the intensities of the NO_x-related vibrational features of the sulfur-free surface (black spectrum) drastically decrease indicating blocking of the NO_x adsorption sites with SO_x due to severe poisoning. This behavior, though not as severe as the Pt/20BaO/Al case (Fig. 11d), is also observed to a certain extent for the Pt/20BaO/AZT catalyst (Fig. 11c). These findings are in good agreement with the NSC trends for fresh and poisoned monolithic catalysts presented in Fig. 7a and b.

Conclusions

In the current study, advanced quaternary mixed oxide materials in the form of $BaO/Al_2O_3/ZrO_2/TiO_2$, functionalized with Pt active sites, were synthesized and structurally characterized *via* XRD and BET in comparison to a conventional Pt/20BaO/Al benchmark NSR/LNT catalyst. The interactions of these catalysts' surfaces with SO_x and NO_x gases were monitored using spectroscopic techniques such as *in situ* FTIR and TPD in order to investigate the nature of the adsorbates on these particular catalysts. The NSC of these catalysts was also measured under realistic flow reactor measurements after sulfur poisoning, and subsequent regeneration. Unlike the conventional Pt/20BaO/Al benchmark catalyst, the Pt/8BaO/AZT and Pt/20BaO/AZT catalysts reveal disordered structures lacking well-crystallized phases. In addition to the direct correlation between BaO loading and NSC, increasing the BaO loading in the Pt/BaO/AZT system increases the thermal stability of the generated bulk and surface sulfate/sulfite species after sulfur poisoning which, in turn, necessitates the use of higher reduction temperatures for complete sulfur elimination with $H_2(g)$. There seems to be a delicate trade-off between the NO_x storage capacity (NSC) and sulfur uptake/poisoning which is strongly governed by the BaO loading/dispersion as well as the surface structure of the support material. It is apparent that although high BaO loadings favor higher NSC, they also render the NSR/LNT catalyst to be more prone towards sulfur poisoning. Thus, by designing a catalyst with an appropriate support material (*e.g.* AZT) that is functionalized with 20 wt% BaO, a sulfur-tolerant NSR/LNT system with satisfactory NSC was achieved. Among all of the examined catalysts, flow reactor experiments revealed that Pt/20BaO/AZT possessed a superior NSC at 573 K to that of the conventional Pt/20BaO/Al benchmark both as a fresh catalyst as well as after poisoning and subsequent regeneration at 773 and 973 K. Surface acidity characteristics of Pt/20BaO/AZT revealing a unique concentration and strength of Lewis and Brønsted acid sites seem to be an important factor for the superior NSR/LNT performance of this catalytic material.

Notes and references

1 S. Roy and A. Baiker, *Chem. Rev.*, 2009, **109**, 4054–4091.
2 W. S. Epling, L. E. Campbell, A. Yezerets, N. W. Currier and J. E. Parks, *Catal. Rev.: Sci. Eng.*, 2004, **46**, 163–245.
3 S. Matsumoto, *CATTECH*, 2000, **4**, 102–109.
4 K. Kato, H. Nohira, K. Nakanishi, S. Iguchi, T. Kihara and H. Muraki, *Euro Patent Application*, 0,573,672 A1, 1993.
5 N. Myioshi, S. Matsumoto, K. Katoh, T. Tanaka, K. Harada, N. Takahashi, K. Yokota, M. Sugiura and K. Kasahara, *SAE Tech. Pap. Ser.*, 1995, 950809.
6 M. P. Ruggeri, T. Selleri, M. Colombo, I. Nova and E. Tronconi, *J. Catal.*, 2014, **311**, 266–270.
7 H. Lindholm and L. Sjövall, *Appl. Catal., B*, 2010, **98**, 112–121.
8 Z. Say, E. I. Vovk, V. I. Bukhtiyarov and E. Ozensoy, *Top. Catal.*, 2013, **56**, 950–957.
9 G. S. Senturk, E. I. Vovk, V. I. Zaikovskii, Z. Say, A. M. Soylu, V. I. Bukhtiyarov and E. Ozensoy, *Catal. Today*, 2013, **184**, 54–71.
10 N. Takahashi, H. Shinjoh, T. Iijima, T. Suzuki, K. Yamazaki, K. Yokota, H. Suzuki, N. Miyoshi, S. Matsumoto, T. Tanizawa, T. Tanaka, S. Tateishi and K. Kasahara, *Catal. Today*, 1996, **27**, 63–69.
11 C. Sedlmair, K. Seshan, A. Jentys and J. A. Lercher, *Catal. Today*, 2002, **75**, 413–419.
12 E. Kayhan, S. M. Andonova, G. S. Senturk, C. C. Chusuei and E. Ozensoy, *J. Phys. Chem. C*, 2010, **114**, 357–369.
13 S. M. Andonova, G. S. Senturk, E. Kayhan and E. Ozensoy, *J. Phys. Chem. C*, 2009, **113**, 11014–11026.
14 S. M. Andonova, G. S. Senturk and E. Ozensoy, *J. Phys. Chem. C*, 2010, **114**, 17003–17016.
15 E. Emmez, E. I. Vovk, V. I. Bukhtiyarov and E. Ozensoy, *J. Phys. Chem. C*, 2011, **115**, 22438–22443.
16 R. Hummatov, D. Toffoli, O. Gulseren, E. Ozensoy and H. Ustunel, *J. Phys. Chem. C*, 2012, **116**, 6191–6199.

This journal is © The Royal Society of Chemistry 2017

Catal. Sci. Technol., 2017, **7**, 133–144 | 143

17 Z. Say, E. I. Vovk, V. I. Bukhtiyarov and E. Ozensoy, *Appl. Catal., B*, 2013, **142–143**, 89–100.

18 Z. Say, M. Tohumeken and E. Ozensoy, *Catal. Today*, 2014, **231**, 135–144.

19 S. Matsumoto, Y. Ikeda, H. Suzuki, M. Ogai and N. Miyoshi, *Appl. Catal., B*, 2000, **25**, 115–124.

20 I. Hachisuka, H. Hirata, Y. Ikeda and S. Matsumoto, *SAE Tech. Pap. Ser.*, 2000, 011196.

21 H. Y. Huang, R. Q. Long and R. T. Yang, *Appl. Catal., B*, 2001, **33**, 127–136.

22 K. Ito, S. Kakino, K. Ikeue and M. Machida, *Appl. Catal., B*, 2007, **74**, 137–143.

23 T. Kanazawa, *Catal. Today*, 2004, **96**, 171–177.

24 B. M. Reddy and A. Khan, *Catal. Rev.: Sci. Eng.*, 2005, **47**, 257–296.

25 K. Arata, S. Akutagawa and K. Tanabe, *Bull. Chem. Soc. Jpn.*, 1976, **49**, 390–393.

26 I. Wang, W. F. Chang, R. J. Shiau, J. C. Wu and C. S. Chung, *J. Catal.*, 1983, **83**, 428–436.

27 H. Imagawa, T. Tanaka, N. Takahashi, S. Matsunaga, A. Suda and H. Shinjoh, *J. Catal.*, 2007, **251**, 315–320.

28 H. Imagawa, N. Takahashi, T. Tanaka, S. Matsunaga and H. Shinjoh, *Appl. Catal., B*, 2009, **92**, 23–29.

29 H. Imagawa, T. Tanaka, N. Takahashi, S. Matsunaga, A. Suda and H. Shinjoh, *Appl. Catal., B*, 2009, **86**, 63–68.

30 N. Takagi, Y. Sobue, H. Ikeda, M. Kamada and R. Inde, *Euro Patent Application*, 12767402.6, 2014.

31 N. Takahashi, A. Suda, I. Hachisuka, M. Sugiura, H. Sobukawa and H. Shinjoh, *Appl. Catal., B*, 2007, **72**, 187–195.

32 Z. Q. Zou, M. Meng, X. Y. Zhou, X. G. Li and Y. Q. Zha, *Catal. Lett.*, 2009, **128**, 475–482.

33 Z. Say, M. Tohumeken and E. Ozensoy, *Catal. Today*, 2016, **267**, 167–176.

34 Z. Say, M. Dogac, E. I. Vovk, Y. E. Kalay, C. H. Kim, W. Li and E. Ozensoy, *Appl. Catal., B*, 2014, **154–155**, 51–61.

35 C. C. Chang, *J. Catal.*, 1978, **53**, 374–385.

36 H. C. Yao, H. K. Stepien and H. S. Gandhi, *J. Catal.*, 1981, **67**, 231–236.

37 O. Saur, M. Bensitel, A. B. M. Saad, J. C. Lavalley, C. P. Tripp and B. A. Morrow, *J. Catal.*, 1986, **99**, 104–110.

38 M. Kantcheva, I. Cayirtepe, A. Naydenov and G. Ivanov, *Catal. Today*, 2011, **176**, 437–440.

39 C. H. Sedlmair, K. Seshan, A. Jentys and J. A. Lercher, *Catal. Today*, 2002, **75**, 413–419.

40 F. M. Hoffmann, *Surf. Sci. Rep.*, 1983, **3**, 107–192.

41 L. Olsson and H. Karlsson, *Catal. Today*, 2009, **147S**, S290.

42 L. Olsson and E. Fridell, *J. Catal.*, 2002, **210**, 340–353.

43 M. May, J. Navarrete, M. Asomoza and R. Gomez, *J. Porous Mater.*, 2007, **14**, 159–164.

44 J. A. Wang, X. Bokhimi, O. Novaro, T. Lopez, F. Tzompantzi, R. Gomez, J. Navarrete, M. E. Llanos and E. Lopez-Salinas, *J. Mol. Catal. A: Chem.*, 1999, **137**, 239–252.

45 J. Sanchez-Valente, X. Bokhimi and F. Hernandez, *Langmuir*, 2003, **19**, 3583–3588.

46 J. C. Vedrine, A. Auroux, V. Bolis, P. Dejaifve, C. Naccache, P. Wierzchowski, E. G. Derouane, J. B. Nagy, J. P. Gilson, J. H. C. van Hooff, J. P. van den Berg and J. Wolthuizen, *J. Catal.*, 1979, **59**, 248–262.

47 B. M. Reddy, G. K. Reddy, K. N. Rao and L. Katta, *J. Mol. Catal. A: Chem.*, 2009, **306**, 62–68.

48 R. Barthos, F. Lónyi, G. Onyestyák and J. Valyon, *J. Phys. Chem. B*, 2000, **104**, 7311–7319.

49 M. Łaniecki, M. Małecka-Grycz and F. Domka, *Appl. Catal., A*, 2000, **196**, 293–303.

50 F. Arena, R. D. Chio and G. Trunfio, *Appl. Catal., A*, 2015, **503**, 227–236.